

# 3D Augmented Fluoroscopy in Interventional Neuroradiology: Precision Assessment and First Evaluation on Clinical Cases

Sébastien Gorges\*

GE Healthcare, Buc, France

INRIA-LORIA, Villers-les-Nancy, France

Erwan Kerrien and Marie-Odile Berger

INRIA-LORIA, Villers-les-Nancy, France

Jérémie Pescatore and Yves Troussel

GE Healthcare, Buc, France

René Anxionnat, Serge Bracard and Luc Picard

Diagnostic and Therapeutic Neuroradiology Dept, University Hospital of Nancy, France

## ABSTRACT

To improve the tool (guide wire and catheter) guidance in interventional radiology, a new approach is to project 3D X-ray Angiography (3DXA) information in real time onto a fluoroscopy image ("*3D Augmented Fluoroscopy*" - 3D AF). Recovering the acquisition geometry is a crucial step for such augmented reality application. As 3DXA and fluoroscopy images are acquired on the same vascular C-arm, a machine-based 3D-2D registration is possible. The feasibility of such an approach was proved and demonstrated in [1]. As a result, a complete Augmented Reality (AR) system, which enables to superimpose the 3DXA onto real time fluoroscopy images is going to be developed and installed in one of the vascular room of our institution. The system promises to help the radiologist to guide the tool to the pathology to be treated without the need to inject contrast medium. The X-ray dose, injected volume of contrast agent, procedure time and patient discomfort are expected to be reduced.

This paper extends our previous work [1] in two ways. First, the study to assess the precision of the machine-based registration is completed, including various C-arm orientations and different focal lengths. A mean 2D error of 1 mm was observed. Secondly, a preliminary clinical evaluation of the AR system is reported and clinical evaluation grid is proposed as a ground to an objective and perceptual evaluation of such an AR application implying many observers and patient cases.

This study demonstrates the potential of the 3D AF to improve navigation in interventional radiology.

**Keywords:** Medical Augmented Reality, Interventional Radiology, 3D/2D Registration, Calibration

## 1 INTRODUCTION

Many cerebro-vascular pathologies can now be operated in a minimally-invasive way thanks to interventional neuroradiology (based on the use of a vascular C-arm). During the intervention, the radiologist may acquire Digital Subtracted Angiography, or DSA (see Figure 1.a), images showing the arteries, enhanced by injecting a radio-opaque contrast agent. Besides, catheter guiding (navigation) and deployment of tools are performed under visual feedback

\*corresponding author : Sébastien Gorges, e-mail: sebastien.gorges@med.ge.com, sebastien.gorges@loria.fr. Tel :(+33)3-54-95-85-07. Contact Address : INRIA Lorraine, 615 rue du jardin botanique, BP 101, 54602 Villers CEDEX, France

of real-time (30 fps) low-dose X-ray images, called fluoroscopy images. The acquired raw fluoroscopy images (see Figure 2.a) enable to show high-contrast materials located in the imaged region of interest (such as tools and bone). The patient's vessels are not visible on the sequence but for evanescent shots of contrast medium that rapidly flow through the vessels.

To show the tools in relationship with the patient's vasculature for a large period of time, real time fluoroscopy images are subtracted from a mask image of the vessels acquired using contrast medium. This application, called 2D roadmap, (see Figure 2.b) presents some well-known limitations:

- Any change in the C-arm orientation and table position makes the roadmap useless and requires again the injection of contrast agent;
- The image quality is reduced compared to DSA;
- The 2D roadmap does not provide any 3D information. The navigation requires a mental reconstruction of the patient's vessels and tool.

Today, 3D X-ray angiography (3DXA, see Figure 1.b) is widely available on vascular C-arms. For these tomographic reconstructions, a set of 2D X-ray images is acquired during a high speed C-arm rotation around the patient's head. Such 3D images are recognized as being of a daily clinical usefulness for the planning and follow-up of the treatment of cerebral pathologies [2].

An improvement over 2D roadmap would be to leverage the high-resolution volumetric information provided by 3DXA to complement fluoroscopy images and ease the tool guidance. Thus, the raw fluoroscopy image could be augmented by projecting the 3DXA information in real time onto it ("*3D Augmented Fluoroscopy*", or *3D AF*) [1] instead of using an injected 2D X-ray mask image. Such an approach requires registering 3DXA with fluoroscopy images for any orientation of the C-arm.

Both images to be registered are acquired on the same machine. Under the hypothesis of no patient motion, previous works [1, 3, 4, 5] showed that registration can be deduced from the information provided in real-time by the system sensors, such as the C-arm angles. Feasibility results were presented in [1], and it was shown that to have an accurate superimposition, machine-based registration should include the mechanical deformations undergone by the vascular C-arm [6].

A complete Augmented Reality (AR) system, which enables the superimposition of the 3DXA onto real time fluoroscopy images is going to be developed and installed in one the vascular room of our institution. The system promises to help the radiologist guide the tool to the pathology by showing the 3D information with respect to the 2D tool position. Moreover, the automatic machine-based registration is expected to overcome some limitations of the

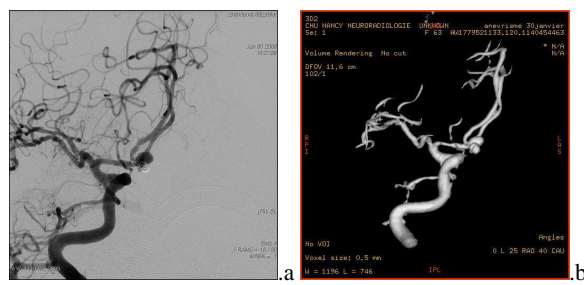


Figure 1: Interventional neuroradiology images showing the patient's vessels: DSA image (a) and 3DXA volume rendering (b)

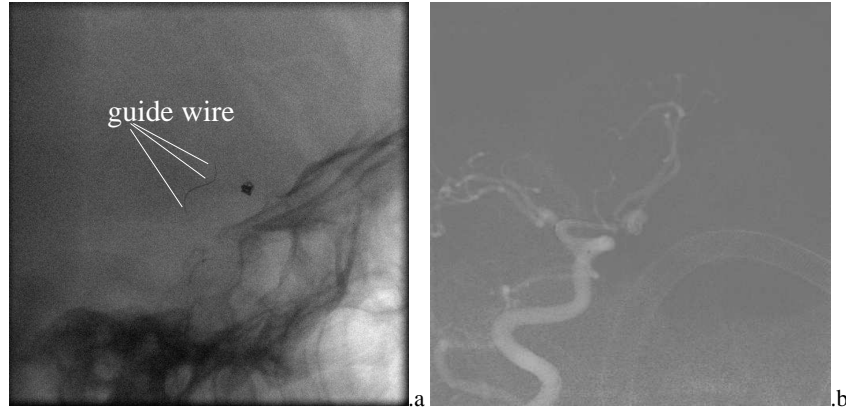


Figure 2: Fluoroscopy images: raw fluoroscopy image showing the guide wire (a) and 2D roadmap image (b).

2D roadmap. With 3D AF, the superimposition is available for any C-arm orientation and for multiple focal lengths without needing to inject. As a result, the injected volume of contrast medium, procedure time and consequently, patient discomfort and X-ray dose are expected to be reduced.

Very few AR systems are in practice deployed at clinical sites and evaluated by the medical doctors. Therefore, the registration precision obtained in clinical conditions and the clinical improvement brought by the AR system are difficult to evaluate. Reports of AR systems already developed [7, 8, 9], showed that clinical evaluation is a crucial step to validate clinical hypotheses (eg. rigid organ behavior, patient and respiratory negligible motion) and clinical improvement in terms of precision and procedure time. Nicolau, in [9], reevaluated the effective precision of his AR system to guide a needle in real clinical conditions. To achieve a relevant AR system, Edwards [7] showed that precision assessment and clinical evaluation have to be done as part of the design and validation of the system.

Concerning 3D AF, Söderman in [10], started the very first step of the clinical validation. This evaluation is a report of clinical cases which were treated with a similar technique. No precision assessment and graduated evaluation were done. However, the procedure time and the injected volume of contrast agent were reduced.

In this paper, the aim was twofold: on the one hand, to understand if the achieved quality of machine-based registration is sufficient for clinical use and on the other hand, to evaluate if 3D augmented fluoroscopy has the potential to improve the navigation of tools compared to classical 2D roadmap. Extending our previous work, greater efforts were done to assess the effective precision of the machine-based registration (including multiple focal length of the vascular C-arm). The paper also presents the preliminary clinical

evaluation of 3D AF in the treatment of intracranial aneurysms.

To perform this study, navigation data have been collected on 3 different cases of intracranial aneurysm treatment. Then, 2 senior radiologists retrospectively analyzed "off line" some clinical aspects of 2D roadmap and 3D AF.

The paper is organized as follows. Section 2 provides a general description of the vascular C-arm and its sensors. Then, machine-based 3D-2D registration approaches are presented in section 3. In section 4, the quantitative quality of the machine-based registration is evaluated. The validation study of our AR solution and results are presented and discussed in section 5. Conclusion and suggestions for future work are presented in section 6.

## 2 THE VASCULAR C-ARM

### 2.1 The C-arm sensors

During a clinical procedure, the C-arm can be oriented in any incidence (Figure. 3). The orientation is classically described by two anatomical angles:  $\alpha$  = cranio-caudal and  $\beta$  = right/left anterior orientation. A given orientation is reached by activating two independent motors impacting a rotative motion along the  $\alpha$  axis and  $\beta$  axis respectively. Furthermore, the imager is mounted on a lift which can be translated to adjust its distance to the X-ray tube (Source to Image Distance, or SID). The SID and the  $\alpha$  and  $\beta$  angles are measured in real time by sensors.

### 2.2 The acquisition geometry

In the latest generation of vascular C-arms, the detector is a flat panel detector, which is free from geometric distortion. Therefore, the acquisition geometry is only modeled as a pinhole camera by a

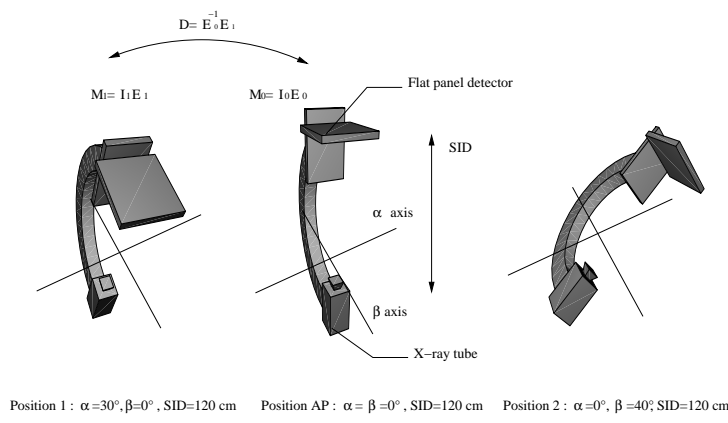


Figure 3: The vascular C-arm: The change in the acquisition geometry  $\mathbf{M}$  is given by the rigid motion  $\mathbf{D}$

projection matrix which gives for each point  $X$  of the 3D space its corresponding projection  $q$  in the acquired 2D image:

$$sq = \mathbf{M}\mathbf{X} \quad \text{with} \quad \mathbf{M} = \begin{bmatrix} m_{11} & m_{12} & m_{13} & m_{14} \\ m_{21} & m_{22} & m_{23} & m_{24} \\ m_{31} & m_{32} & m_{33} & m_{34} \end{bmatrix}$$

with  $s$  a scaling factor.

### 2.3 The intrinsic and extrinsic parameters

The projection matrix can be decomposed into two sets of acquisition parameters and viewed as a combination of two geometrical transformations:

$$\mathbf{M} = \mathbf{K}\mathbf{E} = \begin{bmatrix} \alpha & 0 & u_0 \\ 0 & \alpha & v_0 \\ 0 & 0 & 1 \end{bmatrix} [\mathbf{R}|\mathbf{T}]$$

The *intrinsic parameters*  $\mathbf{K}$  describe the projection parameters from the X-ray tube to the 2D view:  $(u_0, v_0)$  is the principal point and  $\alpha$  is the focal length in pixels (square pixels); the *extrinsic parameters*  $\mathbf{E}$  define the orientation  $\mathbf{R}$  and position  $\mathbf{T}$  of the acquisition system in a world coordinate system.

### 2.4 The classical "off line" calibration procedure

In most applications, an X-ray image of a 3D calibration phantom is acquired and correspondences are established between 3D points of the calibration phantom and their 2D projection in the image. Then,  $\mathbf{M}$  is estimated through the minimization of the reprojection error  $\mathcal{E}_r$  [11]:

$$\mathcal{E}_r(\mathbf{M}) = \frac{1}{n} \sum_{i=1}^n \|\mathbf{M}\mathbf{X}_i - q_i\|^2 \quad (1)$$

where  $n$  is the number of detected markers  $q_i$  in the image and  $\mathbf{X}_i$  are the coordinates of the 3D markers.

The projection matrices obtained by this method are used as the gold standard in this paper and the real time machine-based registration will be compared to it.

The estimated projection matrix is known with a sub-pixel reprojection error, however such an approach requires each position that will be used during the treatment to be calibrated. In practice, these positions are not predictable and thus can not be pre-calibrated.

In the next section, the real time recovery of the projection geometry is discussed in the framework of machine-based registration.

## 3 MACHINE-BASED 3D-2D REGISTRATION

In this section, we define the concept of machine-based 3D-2D registration to determine with a sufficient accuracy the acquisition geometry. First the state of the art is discussed and the limitations of previous approaches are shown. Based on the results of our previous work [1], a model including C-arm deformations is proposed and a calibration procedure is discussed.

### 3.1 State of the art

Machine-based 3D-2D registration approaches [3, 4, 5] all aim at estimating the intrinsic and extrinsic parameters, thus building up the  $\mathbf{M}_{\alpha,\beta}$  matrix by the knowledge of machine sensors:

$$\mathbf{M}_{\alpha,\beta} = \mathbf{K}_{\alpha,\beta} \mathbf{E}_{\alpha,\beta}$$

The intrinsic parameters  $(u_0, v_0)$  are assumed constant while  $f$  directly depends on the SID.

The extrinsic parameters  $\mathbf{E}_{\alpha,\beta}$  are recovered by modeling the rigid motion of the C-arm from a reference orientation ( $\alpha = \beta = 0$ , ie. the Antero-Posterior Position or AP) to  $(\alpha, \beta)$  (see Figure 3). Under the hypothesis that the  $\alpha$  and  $\beta$  motions are independent, this rigid motion  $\mathbf{D}$  is a composition of two rigid motions:  $\mathbf{D}_\alpha$  around the  $\alpha$  axis, and  $\mathbf{D}_\beta$  around the  $\beta$  axis:

$$\mathbf{E}_{\alpha,\beta} = \mathbf{E}_0 \mathbf{D} \quad \text{with} \quad \mathbf{D} = \mathbf{D}_\alpha \mathbf{D}_\beta$$

where  $\mathbf{E}_0 = [\mathbf{R}_0 | T_0]$  are the extrinsic parameters in the reference orientation.

Dumay [3] modeled  $\mathbf{D}$  as made of two independent rotations around the  $\alpha$  and  $\beta$  axes respectively. Both axes were assumed to be *a priori* known, orthogonal and to intersect at the isocenter point.

Kerrien [4] showed that the hypotheses of Dumay were not valid and proposed to calibrate the axes of rotation.

Cañero [5] compared 4 models with growing complexity, starting from Dumay's model, and showed significant improvements in the accuracy of the registration.

Still, the C-arm bears slight mechanical bendings that impair the accuracy of the previous models. To assess these deformations, methods to get reliable and independent measurements of intrinsic and extrinsic parameters were proposed in [6].

An important residual translation of the image chain and a motion of the principal point were thereby measured during a  $\beta$  rotation. These may be interpreted as a physical change of the relative position between the X-ray tube and the flat panel, and a global

mechanical bending of the C-arm under its own weight in lateral positions.

According to the C-arm behavior, *a posteriori* models taking the mechanical behavior of the vascular C-arm into account were proposed in [1]. Both models gave similar results in terms of reprojection error and we selected for this evaluation the simplest one which assumes constant intrinsic parameters.

### 3.2 Parameters of the machine-based registration

In this model,  $\mathbf{D}_\alpha$  is a rotation of angle  $\alpha$ , given by the sensor, and parameterized by an axis vector  $\vec{v}_a$  and a fixed point  $C_a$ .  $\mathbf{D}_\beta$  is a rotation of angle  $\beta$ , given by the sensor, and parameterized by an axis vector  $\vec{v}_b$  and a fixed point  $C_b$  associated to a translation along  $\vec{v}_b$  of amplitude  $\lambda$ . Second- and third-order polynomials were tested to model the variation of parameter  $\lambda$  as a function of  $\beta$ . The latter gave better results:  $\lambda = \sum_{i=0}^3 \lambda_i \beta^i$

The intrinsic parameter  $(u_0, v_0)$  is constant. The pixel size is known and the focal length  $f$  is modeled as equal to the SID up to a constant  $c$ . This constant is known as soon as the focal length  $f_{ref}$  in a reference position is calibrated:  $c = f_{ref} - SID_{ref} = f - SID$ . The model is parameterized by:

$$\phi = \{\mathbf{R}_0, T_0; \vec{v}_a, C_a; \vec{v}_b, C_b, (\lambda_i)_{i=0..3}; u_0, v_0, f_{fref}\}$$

### 3.3 Calibrating the model

To predict in real time the projection geometry  $\mathbf{M}$  by the knowledge of the machine sensors, the parameter vector  $\phi$  has to be calibrated in an off line procedure.

We proposed to perform this task following the multi-image calibration procedure to avoid compensating effects between the parameters.

#### 3.3.1 Multi-image calibration [12]

This is well-known in computer vision that although the projection matrix estimated thanks to the classical method (as described in section 2.4) is known with a sub-pixel reprojection error, its decomposition into intrinsic and extrinsic parameters is unstable. This is due to the instability of the equation used to calibrate the acquisition geometry (coupling effects between intrinsic and extrinsic parameters) and to the noise affecting the 2D and 3D measurements of the landmarks of the calibration phantom.

Puget and Skorda in [13] showed that the variation of the intrinsic parameters can reach 25 pixels for a camera with a fixed focal length using the calibration method.

In order to reduce the statistical noise affecting the set of parameters, calibration can be repeated with varying extrinsic parameters and fixed intrinsic parameters. Thereby, the inter-dependence between both sets of parameters is reduced, so that reliable calibration parameters are estimated. In [12], the camera is moved around the calibration target assuming constant intrinsic parameters. The common intrinsic parameters  $\mathbf{K}$  and  $N$  extrinsic parameters  $(\mathbf{E}_i)$  are then estimated simultaneously by minimizing the residual reprojection error  $\mathcal{R}_m$  on the  $N$  images, using Levenberg-Marquardt algorithm:

$$\mathcal{R}_m = \frac{1}{N} \sum_{i=1}^N \mathcal{E}_r(\mathbf{M}_i) \quad \text{with} \quad \mathbf{M}_i = \mathbf{K}\mathbf{E}_i \quad (2)$$

#### 3.3.2 Calibration procedure

Since intrinsic parameters are considered constant in this model, a classical multi-image calibration has been performed to reduce the statistical noise affecting the vector of parameters  $\phi$ . Therefore, images of the calibration phantom are acquired with a moving C-arm

and a fixed calibration phantom around some calibration position. One image is acquired for every orientation of a set of calibration orientation called  $\mathcal{R}$  in what follows (see section 4.1).

The only difference with the classical multi-image calibration procedure is that the  $N$  extrinsic parameters are replaced by the components of  $\phi$  modeling the extrinsic parameters while the intrinsic parameters are kept constant. The solution vector is given by :

$$\phi = \underset{\mathcal{R}}{\operatorname{argmin}} \left( \frac{1}{N_p} \sum \mathbf{K}\mathbf{E}_{\alpha,\beta} \right)$$

where  $N_p$  is the number of calibration positions.

## 4 QUANTITATIVE PRECISION ASSESSMENT

The various validation studies that follow were targeted to 3D AF. As a result, the 2D reprojection error (see equation 1) was chosen as the figure of merit to evaluate the precision of the acquisition geometry given by the model.

As described in section 2.4, the gold standard method to get the geometry of a given C-arm orientation is to use a calibration phantom and to pre-calibrate this orientation. Then, the C-arm can be positioned again in this orientation thanks to the sensor information (angles and SID) with a given error that will be called C-arm repositioning error.

First, in section 4.2, the repositioning error of the vascular C-arm was assessed. Such measurements show the absolute limit of precision of 3D AF : the best that we can do is to pre-calibrate a predefined position. Then, the precision of our predictive model was evaluated and compared to the repositioning precision. To conclude, the visual impact of the machine-based registration was evaluated with a phantom of aneurysm.

### 4.1 Experimental setup

Our medical institution is equipped with a vascular C-arm mounted with the latest generation of flat panel detectors (INNOVA 4100 – GE Healthcare, Buc, France), thus bearing no geometrical distortions. The pixel size is 0.2 mm with a field of view of 20 cm.

For each  $\alpha$  and  $\beta$  axis, 5 orientations were chosen according to each axis of rotation:  $\mathcal{P}_\alpha = \{(\alpha, \beta) | \beta = 0 \text{ \& } \alpha \in [-30^\circ, -20^\circ, -10^\circ, 0^\circ, 10^\circ, 20^\circ, 30^\circ]\}$  and  $\mathcal{P}_\beta = \{(\alpha, \beta) | \alpha = 0 \text{ \& } \beta \in [-90^\circ, -60^\circ, -40^\circ, -10^\circ, 0^\circ, 10^\circ, 40^\circ, 60^\circ, 90^\circ]\}$ . The  $\mathcal{R}$  set of orientations is defined by :  $\mathcal{R} = \mathcal{P}_\alpha \cup \mathcal{P}_\beta$ . For the experiments, the calibration phantom was positioned onto the table in order to be visible in each frame of the  $\mathcal{R}$  set.

### 4.2 Repositioning experiment

For each orientation of the  $\mathcal{R}$  set, keeping a fixed SID, 3 X-ray images of the calibration phantom were acquired moving the C-arm between 2 image acquisitions. The repositioning error of the C-arm can be detected through the appeared motions of the phantom landmarks between 2 images. For each pair of images in the same orientation, the average landmark motion was computed, leading to 3 measurements per orientation. For each orientation, the 3 measurements were averaged, giving the repositioning error for that orientation.

The same acquisition procedure was performed with 3 different SID: SID=104.5, 114.5 and SID=95 cm.

The statistics of the repositioning error are reported in Table 1. Results show that, if the C-arm is moved to a pre-calibrated orientation, the projection geometry can be known with a mean 2D error of 0.6 mm (whatever the focal length of the system). This value is the limit of precision for 3D augmented fluoroscopy application.

	SID		
	114.5 cm	104.5 cm	95 cm
mean (mm)	0.61	0.58	0.6
std (mm)	0.40	0.35	0.37
max (mm)	1.0	0.97	1.02
min (mm)	0.05	0.09	0.05

Table 1: Statistics about the distance between landmarks

$\alpha(^{\circ})$	$\beta(^{\circ})$	error (mm)
0	10	0.1
0	40.3	0.18
0	60.2	0.26
0	90	0.36
0	-10.2	0.13
0	-39.5	0.36
0	-60.1	0.24
0	-80.3	0.16
0	-90	0.2
-9.9	0	0.15
-20.2	0	0.29
-29.8	0	0.33
-40.9	0	0.43
10.4	0	0.11
19.7	0	0.34

Table 2: Reprojection error (simple C-arm orientations) for the matrices predicted by the C-arm model. The mean error was 0.25 mm (std=0.1).

### 4.3 Machine-based registration error assessment

To measure the error of the machine-based registration in a given C-arm position, an x-ray image of the calibration target is acquired, then the reprojection error between the detected landmarks and the acquisition geometry (given by the machine based registration) is computed. This error was studied according to multiple C-arm orientations and focal lengths. We defined a "simple C-arm orientation" when the C-arm was moved either around  $\alpha$  or around  $\beta$  exclusively and a "complex C-arm orientation" when the motion was both around  $\alpha$  and  $\beta$ .

#### Experiment 1: fixed SID

The parameters of the model were calibrated as described in section 3.3.2 using the  $\mathcal{R}$  set of C-arm orientations and keeping a fixed SID (=118 cm). Images of the calibration phantom were also taken in other C-arm orientations for validation purpose (with the same value of SID). The test set is divided into simple C-arm orientations (see Table 2) and complex orientations (see Table 3).

Results of the experiment are shown in Tables 2 and 3. The precision of the model was very good for simple C-arm orientations. Indeed, the mean error was below 0.5 mm in 100% of the test set. Concerning "complex C-arm orientations" (Table 3), it appeared that the mean error was equal to 0.7 mm which is a value comparable to the repeatability precision.

#### Experiment 2: Variable SID

Again, the parameters of the model were calibrated using the  $\mathcal{R}$  set but an intermediary focal length was taken (chosen between the maximum and the minimum range of SID possible values, SID=104.5 cm). Images of the calibration phantom were also taken

$\alpha(^{\circ})$	$\beta(^{\circ})$	error (mm)
10	15.4	0.22
10	30.3	0.36
-19.7	-20.4	0.4
-30.4	59.8	1.05
-39.8	50.4	1.38
-39.8	-20.3	0.58
-15.1	15.4	0.38

Table 3: Reprojection error (complex C-arm orientations) for the matrices predicted by the C-arm model. The mean error was 0.7 mm (std=0.42).

$\alpha(^{\circ})$	$\beta(^{\circ})$	error (mm)
0	0	0.01
0	-9.8	0.03
0	-39.5	0.1
0	-60.2	0.18
0	-89.8	0.26
0	-80.9	0.25
0	10.3	0.41
0	40.1	0.33
0	60.1	0.27
0	89.5	0.33
9.8	0	0.08
20	0	0.15
29.6	0	0.23
-9.8	0	0.18
-19.6	0	0.23
-29.6	0	0.29

Table 4: Residual error of the C-arm model (SID=104.5 cm). The mean error was 0.2 mm (std=0.12).

for other C-arm orientations for validation purpose. The test set was divided into 3 sets:

- Test set 1: C-arm orientations used to calibrate the model (see Table 4).
- Test set 2: Simple C-arm orientations were taken with different values of SID (see Table 5).
- Test set 3: Complex C-arm orientations outside  $\mathcal{R}$  and/or for different SID values from the calibration set (see Table 6).

Results are reported in Tables 5 and 6. Table 5 shows that the model of SID enabled to predict the acquisition geometry with a mean precision of 0.66 mm when the C-arm was positioned in simple C-arm orientations (even if the SID was changed). With complex C-arm orientations (see Table 6) the error was superior but the mean error remained smaller than 1 mm. The visual effect of such an error was evaluated in the following experiment.

### 4.4 Phantom experiment

A silicon phantom of the cerebral vasculature was injected with a contrast agent and a 3DXA was acquired. Then, one fluoroscopy image was taken for 2 C-arm orientations ( $P_1$ :  $\alpha = 8.8^{\circ}$  and  $\beta = 41.1^{\circ}$  and  $P_2$ :  $\alpha = -40.4^{\circ}$  and  $\beta = 28.8.1^{\circ}$  while SID was 118 cm). 3D augmented views were generated, using the C-arm model, to allow for a visual assessment of the local reprojection error to complement the above global statistics. In Figure 4.a and 4.d

SID (cm)	$\beta(^{\circ})$	$\alpha(^{\circ})$	error (mm)
114.5	0	0	0.56
114.5	-9.8	0	0.62
114.5	-39.5	0	0.82
114.5	-60.2	0	0.91
114.5	-89.8	0	1.26
114.5	-80.3	0	1.07
114.5	10.3	0	0.24
114.5	40.1	0	0.33
114.5	60.1	0	0.34
114.5	89.5	0	0.76
114.5	0	9.8	0.58
114.5	0	20	0.6
114.5	0	29.6	0.62
114.5	0	-9.8	0.67
114.5	0	-19.6	0.68
114.5	0	-29.6	0.78
95	0	0	0.5
95	-9.8	0	0.57
95	-39.5	0	0.88
95	-60.2	0	1.11
95	10.3	0	0.75
95	40.1	0	0.55
95	60.1	0	0.47
95	0	9.8	0.62
95	0	20	0.74
95	0	29.6	0.84
95	0	-9.8	0.41
95	0	-19.6	0.42

Table 5: Reprojection error for the matrices predicted by the model the when C-arm orientations only differs from the calibration set by the value of the SID. The mean error was 0.66 mm (std=0.24).

SID	$\beta(^{\circ})$	$\alpha(^{\circ})$	error (mm)
109.7	0	0	1.04
99.5	-39.5	0	0.84
109.5	-89.8	0	1.04
101.9	10.3	0	1
107.6	60.1	0	0.76
111.9	0	9.8	1.07
97.5	0	29.6	0.98
112.4	0	-19.6	1.12
110	-9.8	0	1.05
100.1	-60.2	0	0.8
110.1	-80.3	0	1.01
102.2	40.1	0	0.89
108.4	89.5	0	0.67
112	0	20	1.04
111.5	0	-29.6	1.11
104.5	7.3	0	0.96
104.5	-9.8	-11.3	0.96
118.8	-6.7	28.7	1.23
110.4	28.1	-30.7	1.24
104.9	19.9	13.1	0.95
100.3	-56.4	-13.8	0.93
105.7	23.3	-31.6	1.18

Table 6: Reprojection error for the matrices predicted by the C-arm model. The orientations and SID are different from the calibration set. The mean error was 0.99 mm (std=0.4).

an augmented image is shown. The precision of  $P_1$  position was evaluated (as described above) at 0.45 mm. Superimposition corresponded, from a visual standpoint, to a perfect fit. The precision of  $P_2$  was 1.2 mm. Some very small error can be seen when analyzing the superimposition in Figure 4.d.

## 4.5 Conclusion

The need for precision is very high in interventional neuroradiology. Neuroradiologists are used to navigating in vessels which are smaller than 1 mm. As a consequence, a precision of at least 1 mm was targeted for 3D AF application. A complete error study showed that the mean error was equal to 1 mm when using the C-arm model to predict the acquisition geometry. This was only 0.4 mm greater than the repositioning error. This precision is very encouraging for many medical applications and particularly for 3D AF in interventional neuroradiology. To complement this quantitative measurement of precision, we present in the next section, a first evaluation of clinical interest of 3D augmented fluoroscopy for the treatment of intracranial aneurysms.

## 5 CLINICAL EVALUATION OF 3D AUGMENTED FLUOROSCOPY

The main purpose of this study was to understand if the 2D precision reached by the model was sufficient to allow for efficient 3D AF application in a clinical context. Furthermore, the clinical improvement brought by this new application with respect to the classically used 2D roadmap was also investigated.

### 5.1 System description

During a classical procedure the neuroradiologist uses 3 different displays: first display presents the real time 2D roadmap with moving guide wire or catheter, the second one is classically used to show a reference DSA or 2D roadmap image and the last one is used to display a volume rendering image of the 3DXA.

#### 5.1.1 Classical interventional procedure

Classically, the clinical workflow is as follows. DSA images are acquired and used to localize the pathology to treat. A 3DXA is also acquired and analyzed to understand the 3D structure of the aneurysm. Then, 3DXA is manipulated during the procedure to choose an optimal working view for the treatment. An optimal working view is a view which clears the aneurysm neck and the vessels leading to the aneurysm. Then, under the control of 2D roadmap sequences (acquired under this orientation), the guide wire and the catheter are moved up to the aneurysm. During the navigation, it could happen that the radiologist injects some micro-volume of contrast agent to better see the vessels. Moreover, to perform mental reconstruction of the patient's vessels and better locate the tool with respect to the vasculature, the C-arm can be moved to additional orientations. When the C-arm is moved to a new orientation, additional contrast medium has to be injected for a new 2D roadmap.

#### 5.1.2 3D AF procedure

With our AR solution, an additional display is added in the vascular room showing the 3D AF. The superimposition of 3DXA to the fluoroscopy image is done automatically thanks to our machine-based registration. 3D AF shows the projection of the 3D vessels with respect to the tool position without any injection of contrast agent. The superimposition is available even if the C-arm is moved or the SID changed. The user may change the blending of the 3DXA in

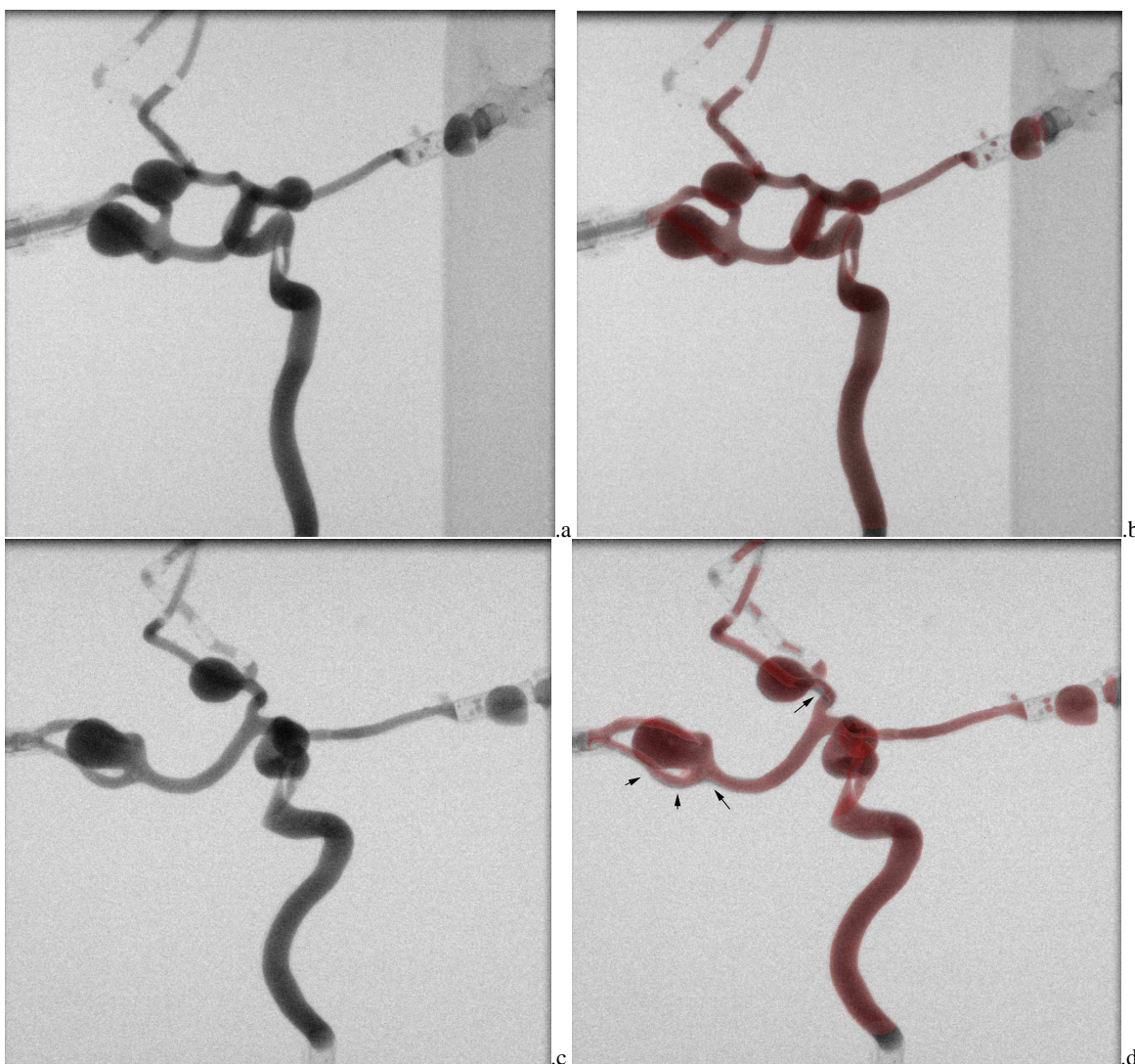


Figure 4: 3D AF on phantom dataset: fluoroscopy image (a,c) and superimposition of the 3DXA onto the fluoroscopy image (b,d). (a,b) was taken with a C-arm positioned at  $\alpha = 8.8^\circ$  and  $\beta = 41.1^\circ$  while (c,d) at  $\alpha = -40.4^\circ$  and  $\beta = 28.8^\circ$ . The arrows show some visible errors.

the fluoroscopy image to better see the tool. Tool visibility is one of the aspects which have to be evaluated.

### 5.1.3 Hypotheses

With our 3D AF solution, the patient is supposed not to move and vessels are supposed not to be deformed during the navigation procedure. According to neuroradiologists, the effect of the guide wire onto the vessels can deform them and lead to imprecision in the navigation procedure. Patient motion and deformation of the vessels can lead to the tool being displayed outside the patient's vasculature. This phenomena is classically observed during navigation using 2D roadmap. An unsatisfying perception could occur if the root cause of the error is not clearly understood by the radiologist during the treatment. Such aspects have to be evaluated.

## 5.2 Methods

Following this analysis, two features appeared as critical for 3D AF in clinical conditions: The radiologist must trust the accuracy

of the image superimposition and the augmented image must bring an effortless understanding of the tool position in 2D and 3D. The following aspects were therefore investigated through an evaluation grid:

### 1. Quality of registration

Based on the superposition of the 3DXA to an injected image, the registration was evaluated for tool guiding, in a scale ranging from bad to good (bad, acceptable, good).

### 2. Registration error

The registration error was usually assessed with respect to the injected image using the following scale:  $\leq 3$  mm or  $\leq 2$ mm or  $\leq 1$ mm or  $\leq 0.5$  mm. The evaluation was done by visually inspecting superimposition of the 3DXA to an injected image. The radiologist used the approximate size of the vessels in the 2D image to visually estimate the 2D error.

### 3. 2D Tool position

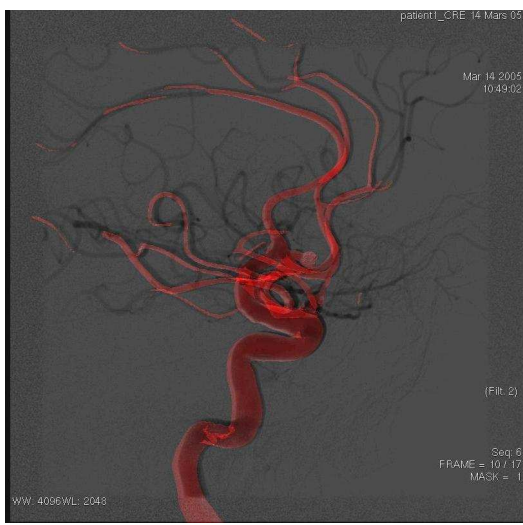


Figure 8: Patient 1. 3DXA superimposed to dsa image

A particular attention was given to assess if the tool was very often, often, sometimes or never outside the vessels. If the tool was detected outside the vessels, the estimated root cause was given by the radiologist. The possibilities were classified as: vessels are deformed, patient moved, tool in a vessel not visible in the image, or error of registration (multiple findings were possible).

#### 4. Tool visibility

The visibility of the guide wire and catheter was also evaluated from bad to good (bad, acceptable, good).

#### 5. 3D tool position

The capability of understanding the 3D position of the guide wire and catheter was evaluated in a scale ranging from bad to good (bad, acceptable, good).

### 5.3 Patients and calibration data

The data used for this evaluation were captured with 3 different patients undergoing an endovascular treatment for an aneurysm. Fluoroscopy and 2D roadmap sequences were captured under the optimal working view orientation while the guide wire guide wire and micro-catheter was moved up to the aneurysm. The duration of the recorded sequences was roughly from 1 to 2 minutes. The C-arm orientations, SID and aneurysm location according to each patient are given in Table 7.

The C-arm model was calibrated as described above using the  $\mathcal{R}$  calibration set of orientations with an SID=104.5 cm. The acquisition geometry was generated with a machine-based registration approach.

Each 3DXA image, fluoroscopy sequence of images and acquisition geometry given by the machine-based registration were then used to generate an "off line" a 3D AF sequence. Some images of the generated sequences are shown in Figures 5, 6 and 7. The 3D augmented fluoroscopy sequences were proposed with 2 different blending factors: the first one was quite low to allow for a good understanding of the 3D anatomy of the patient's vasculature (3D AF surface), while the second was higher in order to facilitate guide wire/micro-catheter visualization (3D AF blending).

Furthermore, to assess the quality of registration, the 3DXA was also superimposed to an injected image taken in the optimal work-

ing view orientation (eg. DSA image or mask image of the 2D roadmap). An example of 3DXA/DSA superimposition is shown in Figure 8.

	$\alpha$ ( $^\circ$ )	$\beta$ ( $^\circ$ )	SID (cm)	Aneurysm location
patient 1	82	5	107	ACA
patient 2	-27	-24	119	ACA
patient 3	5	10	105	MCA

Table 7: Patients used for the validation: C-arm orientations, SID and aneurysm location. ACA = Anterior Communicating Artery, MCA = Middle Cerebral Artery

## 5.4 Results

Two senior neuroradiologists retrospectively analyzed the above parameters independently for 2D roadmap and 3D augmented fluoroscopy. The evaluations given by both observers were very similar, differing at most by 1 scale, leading to a very small inter-observer variability. Thus, we proposed some simple rules to aggregate automatically the answers from the 2 observers, leading to a single score reflecting the satisfaction for aneurysm treatment (see Table 8). A score of 0 (resp 2), is considered to meet (resp exceed) the medical requirements for aneurysm treatment. A value of  $-1$  is considered as encouraging but not satisfying. A score of  $-2$  is considered as unsatisfying.

### 5.4.1 Quality of the registration

The results concerning the quality of the machine-based registration between a 3DXA and an injected 2D X-ray image are given in Table 9. For each patient, classifications indicated that the precision of the 3D/2D registration met the medical requirement for guide wire/micro-catheter navigation. The perception of the error ranges from 1 mm to 0.5 mm.

Evaluation indicated that the guide wire and catheter are most of the time inside the vessels in both applications (3D AF and 2D roadmap). For patients 1 and 2, one observer detected that the guide wire was sometimes outside the vessel but very closed to its wall. According to the observer, this was due to the effect of the tool on the vessels. The same deformation was detected in both applications.

### 5.4.2 Interest of 3D augmented fluoroscopy

According to the observers, the 3D AF blending view always enabled to better see the tool, in terms of contrast, than 3D AF surface view. Also, results from Table 10 show that 3D AF blending was very similar to (or better than, for patient 1) 2D roadmap for tool visibility.

Results in Table 11 indicate that no major difference in the 3D tool position understanding could be noted using 3D AF or 2D roadmap. Observers indicated that the tool visibility with respect

Observer 1	Observer 2	Evaluation
bad	bad	-2
bad	acceptable	-1
acceptable	acceptable	0
acceptable	good	1
good	good	2

Table 8: Rules to aggregate.

	Evaluation	Mean registration error (mm)
patient 1	0	1
patient 2	1	0.75
patient 3	2	0.5

Table 9: Quality of 3DXA-fluoroscopy registration.

	2D roadmap	3D AF surface	3D AF blending
patient 1	-1	-2	0
patient 2	1	-1	1
patient 3	1	0	1

Table 10: guide wire/micro-catheter visibility.

to the vessels was the root cause of this relatively unfavorable evaluation.

To sum up results brought by Tables 10 and 11, if the blending factor is high, the tool is visible but the 3D information brought in the fluoroscopy image is low. In this case, 3D AF is quite similar to the conventional 2D roadmap. The advantage is that no contrast medium has to be injected. In the other hand, if the blending factor is low, the 3D information in the fluoroscopy image is high but the tool visibility is lower than with 3D AF blending and 2D roadmap. Yet according to observer 1, the 3D information with respect to the 2D tool position may help to understand the tool position in some complicated bifurcations. Indeed, for patient 1 the vessels of the MCA/ACA bifurcation are superimposed with 2D roadmap. The bifurcation is easier to understand with 3D AF.

## 6 CONCLUSION

The machine-based registration was evaluated and results showed that this method is able to predict the acquisition geometry for any C-arm orientation with a mean 2D reprojection error of 1 mm whatever the focal length of the system. This accuracy is very encouraging for many medical applications such as 3D augmented fluoroscopy.

A preliminary evaluation was done in a clinical context to assess the precision obtained and to understand the clinical improvements brought by 3D AF.

The evaluation showed that the registration error was perceived as very low and met the medical requirements for tool navigation in interventional neuroradiology. The perception of 2D tool position with respect to the patient's vasculature was evaluated as satisfying and comparable to the classical 2D roadmap. Understanding of the 3D tool position was judged similar to the 2D roadmap. The tool visibility in the 3D AF has to be improved to allow for a better understanding of the relationships between tool and vessels. Improvement of the visualization scheme and tool enhancement could be investigated in future work.

This machine-based approach is a suitable solution for navigation in interventional radiology. Contrary to 2D roadmap, no additional contrast medium has to be injected even if the C-arm is moved or SID changed.

This "off line" evaluation showed that our AR system is valid compared to 2D roadmap. We are now working with "on line" cases to better apprehend the clinical interest of 3D AF and to design in more details the required clinical features.

## REFERENCES

[1] S. Gorges, E. Kerrien, M.-O. Berger, Y. Troussset, J. Pescatore, R. Anxionnat and L. Picard. Model of a vascular C-arm for 3D augmented

	2D roadmap	3D AF surface	3D AF blending
patient 1	-2	-1	-1
patient 2	1	1	1
patient 3	1	1	1

Table 11: Understanding of the tool position.

fluoroscopy. *Proceedings of the 8th Int. Conf. on Medical Image Computing and Computer-Assisted Intervention-MICCAI'05, Palm Spring, US*, 214-222, 2005.

- [2] R. Anxionnat, S. Bracard, X. Ducrocq, Y. Troussset, L. Launay, E. Kerrien, M. Braun, R. Vaillant, F. Scomazzoni, A. Lebedinsky and L. Picard. Intracranial Aneurysms : Clinical Value of 3D Digital Subtraction Angiography in the Therapeutic Decision and Endovascular Treatment. In *Radiology*, (218):799-808, 2001.
- [3] A. Dumay, J. Reiber and J. Gerbrands. Determination of optimal angiographic viewing angles: Basic principles and evaluation study. In *IEEE Trans. on Med. Imag.*, 13(1):13-24, 1994.
- [4] E. Kerrien, R. Vaillant, L. Launay, M.-O. Berger, and E. Maurincomme. Machine precision assessment for 3D/2D digital subtracted angiography images registration. In *Proceedings of the SPIE Medical Imaging'98, San Diego, USA*, 39-49, February 1998.
- [5] C. Cañero, E. Nofrerías, J. Mauri, and P. Radeva. Modeling the acquisition geometry of a C-arm angiography system for 3D reconstruction. In *Conferencia Catalana d'Intel·ligència Artificial - CCIA'2002*, 322-335, 2002.
- [6] S. Gorges, E. Kerrien, M.-O. Berger, Y. Troussset and J. Pescatore. An effective technique for calibrating the intrinsic parameters of a vascular C-arm from a planar target. *Proceedings of the SPIE Medical Imaging'06, San Diego, US, February*, 572-581, 2006.
- [7] P. J. Edwards, A. P. King, C. R. Maurer Jr, D. A. de Cunha, D. J. Hawkes, D. L. G. Hill, R. P. Gaston, M. R. Fenlon, A. Juczyzck, A. J. Strong and C. L. Chandler. Image Guided Surgery - Design and Evaluation of a System for Microscope-Assisted Guided Interventions (MAGI). *IEEE Transactions on Medical Imaging*, pages 1082-1093, 2000
- [8] G. Fichtinger, A. Deguet, K. Masamune, G. Fischer G, Balogh E, Mathieu H, Taylor RH, Fayad LM, SJ Zinreich. Needle Insertion in CT Scanner with Image Overlay - Cadaver Studies. *Proceedings of the 7th Int. Conf. on Medical Image Computing and Computer-Assisted Intervention-MICCAI'04, ST Malo, France*, pages 795-803, 2004.
- [9] S.A. Nicolau, X. Pennec, L. Soler and N. Ayache. A complete Augmented Reality Guidance System for Liver Punctures: First Clinical Evaluation. *Proceedings of the 8th Int. Conf. on Medical Image Computing and Computer-Assisted Intervention-MICCAI'05, Palm Spring, US*, pages 539-547, 2005.
- [10] M. Söderman, D. Babic, R. Homan and T. Andersson. 3D roadmap in neuroangiography: technique and clinical interest. *Neuroradiology*, pages 735-740, 2005
- [11] A. Rougée, C. Picard, C. Ponchut, and Y. Troussset. Geometrical calibration of X-ray imaging chains for three-dimensional reconstruction. In *Computerized Medical Imaging and Graphics*, volume 17(4/5), pages 295-300, 1993.
- [12] J.M. Lavest, M. Viala and M. Dhome. Do we really need an accurate calibration pattern to achieve a reliable camera calibration. In *European Conference on Computer Vision - ECCV'98, Freiburg, Germany*, Vol 1, 158-174, 1998.
- [13] P. Puget and TH. Skordas. An optimal solution for mobile camera calibration. In *European Conference on Computer Vision - ECCV'90, Antibes, France*, volume 17(4/5), pp187-198, 1990.



Figure 5: Patient 1. 2D roadmap (a) versus 3D augmented fluoroscopy with (b) a surface view and (c) a blending view



Figure 6: Patient 2. 2D roadmap (a) versus 3D augmented fluoroscopy with (b) a surface view and (c) a blending view

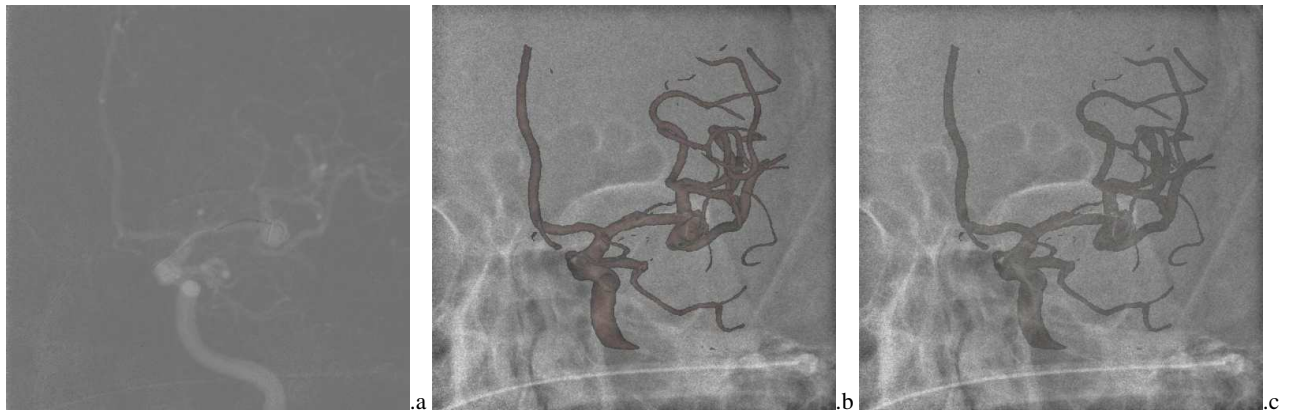


Figure 7: Patient 3. 2D roadmap (a) versus 3D augmented fluoroscopy with (b) a surface view and (c) a blending view